Idealized study of a 2-D coupled sea-ice/atmosphere model during warm-air advection

Bin CHENG, Timo VIHMA

Finnish Institute of Marine Research, P.O. Box 33, FIN-00931 Helsinki, Finland
E-mail: bin@fimr.fi

ABSTRACT. We present a two-dimensional, coupled, mesoscale atmosphere–sea-ice model, and apply it to simulate the air–ice interaction during warm-air advection. The model was run into a steady state under various conditions with respect to the season, cloud cover and wind speed. The spatial and temporal evolution of the thermodynamics of the ice, snow and the atmospheric boundary layer (ABL) were investigated. The development of the stably stratified ABL downwind of the ice edge depended above all on the wind speed and cloud cover. If the turbulent heat flux from air to snow was large enough to compensate the radiative cooling of the surface, a downward conductive heat flux was generated in the upper ice and snow layers. The stronger was the surface heating (strong wind, overcast skies) and the shorter its duration (on a scale down to a few hours), the wider was the region where this downward flux occurred. From the point of view of ABL modelling, the interactive coupling between air and ice was most important when the wind was strong, while from the point of view of ice thermodynamic modelling the coupling was most important when the wind was weak.

1. INTRODUCTION

In polar oceans, the sea ice acts as an insulator between the generally colder atmosphere and the relatively warm ocean. The effectiveness of the insulation depends on the thickness and thermal properties of the ice and snow cover. The thermodynamics of sea ice is usually considered as a one-dimensional process (e.g. Maykut and Untersteiner, 1971). This is a good approach with respect to the heat conduction within the ice and snow. In conditions of a large horizontal temperature gradient in the overlying atmosphere, the effects of this gradient are, however, also reflected in the vertical and horizontal temperature distribution in the sea ice. This is particularly true in the ice-edge zone, where the properties of the marine air mass flowing over the sea ice are modified. During warm-air advection the air is warmer than the snow/ice surface, and the near-surface air mass is therefore cooled via turbulent and radiative fluxes. Simultaneously, the snow or ice surface becomes warmer. The magnitude, spatial scale and temporal evolution of these heating and cooling processes depend on the meteorological situation (e.g. cloud cover, solar radiation, surface albedo, wind speed and air humidity), as well as on the temperatures of the air, snow and ice.

Although a few studies of warm-air advection over sea ice have been published (Andreas and others, 1984; Bennett and Hunkins, 1986; Fairall and Markson, 1987; Kantha and Mellor, 1989; Overland and Guest, 1991; Brümmer and others, 1994), the main interest has been in the processes in the atmospheric boundary layer (ABL). On the other hand, among the numerous studies on sea-ice thermodynamics (e.g. Maykut, 1978; Ebert and Curry, 1993; Schramm and others, 1997) we have not found any with a special emphasis on the spatial variations due to warm-air advection.

On a theoretical basis we can assume that, if the radi-

ative fluxes are small and the turbulent air–ice exchange dominates, the thermal interaction between the surface and the ABL should strongly depend on the fetch over the ice. This is because the turbulent fluxes are sensitive to the snow surface temperature, which is, in turn, affected by the warm-air advection. On the other hand, if the temperatures are below zero and the radiative fluxes dominate, the ice thermodynamics should not be as sensitive to the fetch from the ice edge. This is because the radiative fluxes have a weaker dependence on the snow surface temperature. (The situation changes, however, in melting conditions when the surface albedo is affected.) To test these hypotheses, we have made simulations using a coupled two-dimensional (2-D) ABL–sea-ice model under a variety of idealized meteorological conditions. Our objective is to obtain basic insight into situations of warm-air advection to understand the magnitude, spatial scale and temporal evolution of the thermodynamic processes taking place in the ice-edge zone under different meteorological and surface conditions. Such knowledge can be further applied in atmosphere, ice and ocean models.

2. THE COUPLED MODEL

We simulated the flow over the sea ice using the 2-D ABL model of the University of Helsinki (Alestalo and Savijärvi, 1985; Savijärvi, 1997), which we coupled with a thermodynamic sea-ice model (Cheng, 1996; Launiainen and Cheng, 1998). The structure of the coupled model is shown in Figure 1.

In the ABL part, the flow is forced by a large-scale pressure gradient represented by the geostrophic wind. The model has an (x, σ) coordinate system with 92 points in the horizontal and 50 in the vertical (σ is the atmospheric pressure divided by its surface value). The vertical grid has a quasi-
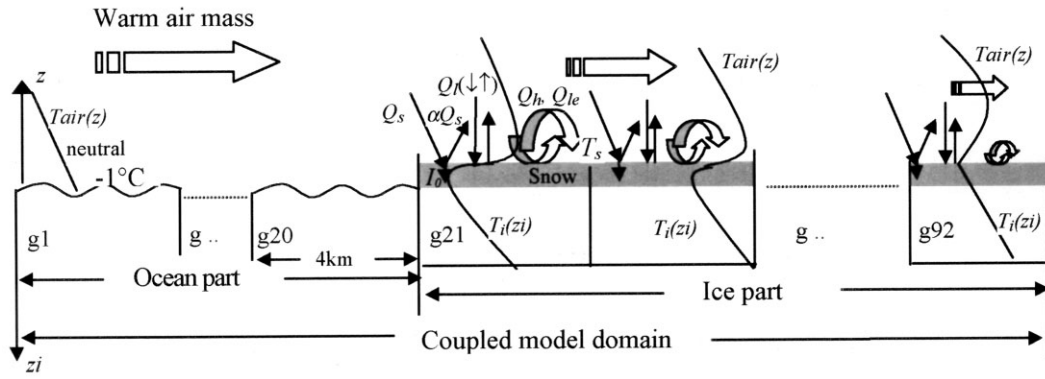
Fig. 1. Structure of the coupled ABL–sea-ice model. The first 20 gridcells (g1–g20) from the inflow boundary represent the open sea with a fixed snow surface temperature and a fixed inflow temperature profile ($\partial T/\partial z = -6.5\,K\,km^{-1}$). The rest of the gridcells (g21–g92) represent sea ice with a snow cover.

logarithmic spacing with the lowest levels at approximately 1.5, 4, 8, 15 and 24 m. The upper boundary conditions are applied at 3 km, where the wind becomes geostrophic. In this study we use a 4 km horizontal grid length with flat topography. The horizontal momentum equation, the hydrostatic equation, the equation of state, the continuity equation, and the conservation equations of heat and moisture compose the core of the ABL model. From the point of view of this study, the heat conservation equation is essential:

$$\frac{\partial \theta}{\partial t} = -u\frac{\partial \theta}{\partial x} - \frac{d\sigma}{dt}\frac{\partial \theta}{\partial \sigma} + \frac{g^2}{p_*^2}\frac{\partial}{\partial \sigma}\left(\rho_a^2 K_z \frac{\partial \theta}{\partial \sigma}\right) + C_0, \quad (1)$$

where θ is the air potential temperature, t is time, u is the horizontal wind component along the model x axis, ρ_a is air density, and g is the acceleration due to gravity. Here, $p_* = p_s - p_t$, in which p_s is the surface pressure and p_t is the pressure at the model top (3 km). C_0 denotes the temperature change due to the release of latent heat of condensation. Turbulence is described by a first-order closure with the vertical diffusion coefficient $K_z = l^2(dU/dz)f(\text{Ri})$, where the mixing length is given by $l = k_0 z/(1 + k_0 z/\varepsilon_0)$. Here, dU/dz is the wind shear, $\varepsilon_0 = 20$ m, k_0 is the von Kármán constant (0.4) and $f(\text{Ri})$ is an empirical function depending on the Richardson number (Ri). In stable stratification, which prevails during warm-air advection over sea ice, $f(\text{Ri}) = \max[0.02, (1-7\text{Ri})]$ is used for momentum, heat and moisture. Vertical diffusion is solved by an implicit method, and instead of explicit horizontal diffusion a weak low-pass filter is applied to all fields (Long and others, 1978; Mahrer and Pielke, 1978). The model dynamics are described in Alestalo and Savijärvi (1985), and the physical parameterizations in Savijärvi (1997). The ABL model has a sophisticated radiation subroutine (a six-band longwave scheme and a four-band two-stream shortwave scheme); but to save computing time in our large set of simulations, we use the simple parameterizations described below.

The ice model is a thermodynamic, vertical, one-dimensional, multi-layer heat- and mass-balance model. The surface heat balance reads

$$(1 - \alpha)Q_s - I_0 + Q_l + Q_h + Q_{le} + F_c + F_m = 0, \quad (2)$$

where Q_s is the downward shortwave radiation at the surface calculated according to Shine (1984) with the cloudiness factor of Bennett (1982) and with α the surface albedo. Q_l is the net longwave radiation: the downward part is calculated according to Prata (1996) with the cloud effect of Jacobs (1978), and the upward part by the Stefan–Boltzmann law. Here, the term I_0 refers to the shortwave radiation penetrat-

ing below the surface layer. F_c is the surface conductive heat flux, and F_m is the heat flux due to surface melting.

The turbulent fluxes of sensible (Q_h) and latent heat (Q_{le}) are calculated by the bulk formulae, i.e. $Q_h = -\rho_a c_p C_H (\theta_s - \theta_z) V_z$ and $Q_{le} = -\rho_a L_v C_E (q_s - q_z) V_z$, in which ρ_a is the air density, c_p is the specific heat and L_v is the enthalpy of vaporization. C_H and C_E are the turbulent transfer coefficients, V is the wind speed and q is the specific humidity. Subscripts s and z refer to the surface and height z in the air, respectively. The temperature θ_z, wind speed V_z, relative humidity Rh and cloudiness are read from the results of the ABL model at the lowest level $z \approx 1.5$ m. C_H and C_E are calculated applying the Monin–Obukhov similarity theory taking into account the stability effects according to Holtslag and de Bruin (1988) in stable cases. An aerodynamic roughness $z_0 = 0.001$ m is used. The thermal roughness length z_T is calculated according to Andreas (1987), which is approximately in agreement with Joffre (1982, 1988) and Launiainen and others (2001).

Below the surface, the ice or snow temperature is solved by a non-linear heat-conduction equation

$$(\rho c)_{sn,i}\frac{\partial T_{sn,i}(z_i, t)}{\partial t} = \frac{\partial}{\partial z_i}\left(k_{sn,i}\frac{\partial T_{sn,i}(z_i, t)}{\partial z_i}\right) - \frac{\partial q_{sn,i}(z_i, t)}{\partial z_i}, \quad (3)$$

where T is the temperature, z_i is the vertical coordinate in ice (positive downward), ρ is the ice or snow density, c is the specific heat and k is the thermal conductivity. Subscripts sn and i denote snow and ice, respectively. The c_i and k_i are considered as functions of ice salinity and temperature following Maykut and Untersteiner (1971). The flux divergence $\partial q(z_i, t)/\partial z_i$ represents the absorbed solar radiation with $q_i(z_i, t)$ parameterized by a two-layer scheme (Launiainen and Cheng, 1998; Cheng, 2002) adopted from Grenfell and Maykut (1977). Alternatively, $q_{sn}(z_i, t) = (1 - \alpha)Q_s\,e^{-\kappa z_i}$ follows the Bouguer–Lambert law, where the extinction coefficient κ varies from 5 m^{-1} for dense snow up to almost 50 m^{-1} for newly fallen snow (Perovich, 1996). The equation is solved by a conservative difference numerical scheme (Cheng, 1996). This scheme is essentially similar to the Crank–Nicholson scheme but with more flexible tuning from explicit to implicit by a single parameter (Cheng and Launiainen, 1998). It is derived by the integral interpolation method, a numerical technique that allows the scheme to be easily extended to an uneven spatial resolution (Cheng, 2002). At the ice bottom, the freezing and melting are controlled by the balance of the conductive heat flux and the oceanic heat flux.

The ice model is coupled with the ABL model at each

horizontal gridpoint. The snow surface temperature (T_s) acts as a key element in the coupling. At each time-step, the snow surface temperature is solved iteratively from Equation (2). The ABL equations are then solved using T_s as a boundary condition, and the resulting V_z, θ_z and Rh_z are forcing inputs for the ice model. The surface heat balance as well as the ice thermal regime are then determined from Equations (2) and (3). Due to the 4 km horizontal grid length in the ABL model, a time-step of 8 s is used.

An exact validation of the two-dimensional coupled ABL–sea-ice model would require an array of ice thermistor strings deployed at an increasing distance from the ice edge. In addition, either aircraft observations or an array of meteorological masts would be required. The coupled model does not, however, account for any horizontal exchange processes inside the ice and snow. Hence, we think that a separate validation of the processes in the ABL (horizontal and vertical) and the (vertical) processes in the ice and snow provides an adequate validation for the coupled model. The ABL model has been validated in Savijärvi (1991), Savijärvi and Kauhanen (2001), Vihma and Brümmer (2002) and Vihma and others (in press), and the sea-ice model in Launiainen and Cheng (1998) and Cheng and others (2001).

3. SIMULATIONS AND RESULTS

3.1. Model set-up

In the model, a horizontal grid of 92 km × 4 km was used. The first 80 km were set as open ocean with a fixed surface temperature of -1°C. The rest of the surface was snow-covered sea ice with an initial snow surface temperature of -30°C. A low temperature was selected to study the maximum effects of a warm-air advection case. A surface albedo of 0.80 was used. The initial ice and snow thicknesses were assumed to be 2.0 and 0.2 m, respectively. In section 3.6 below, we study the sensitivity of the results to the ice concentration, ice thickness and initially warm snow surface temperature.

The snow density and heat conductivity are taken as 450 kg m^{-3} and 0.3 W m^{-1}K^{-1}, which are relevant for hard wind slab or hard drift snow (Sturm and others, 1997). The extinction coefficient of snow is given as 15 m^{-1} (Perovich, 1996). Below the snow, the sea-ice density is assumed to be 900 kg m^{-3}. The thermal conductivity of sea ice is around 2.1 W m^{-1}K^{-1}, depending on ice temperature and salinity. The oceanic heat flux is assumed constant (10 W m^{-2}; Wettlaufer, 1991) and the ice bottom temperature is at the freezing point (-1.8°C).

We fixed the temperature and humidity profiles for the air mass at the inflow boundary over the ocean. The temperature at the lowest grid level (1.5 m) was set equal to the snow surface temperature, and a lapse rate of -6.5 K km^{-1}

Table 1. Boundary conditions in the model runs. Each group included 12 model runs, with the geostrophic wind ranging from 2 to 24 m s^{-1}

Group	Solar radiation	Cloud cover
1	As on 21 March, 70° N (spring equinox)	Clear skies
2	As on 21 March, 70° N (spring equinox)	Overcast
3	No (winter solstice)	Clear skies
4	No (winter solstice)	Overcast

was applied. The inflow relative humidity was set to either 70% (no clouds) or 100% (overcast skies). The geostrophic wind driving the ABL flow varied from 2 to 24 m s^{-1} in the various simulations, and the initial wind profile in the ABL was calculated according to the Ekman–Taylor spiral. In all simulations, the latitude was 70° N, the date was either 21 December (winter solstice) or 21 March (spring equinox), and the model was run for 10 days to reach a steady state or, in the case of the spring simulations, a steady diurnal cycle. The air-temperature field over the ice was initialized by running the model for the first 6 hours with the snow surface temperature fixed at -30°C.

The simulations were organized in four groups (Table 1) with respect to the season (winter or spring) and the cloud cover (clear or overcast skies). Note that each group included 12 model runs with the geostrophic wind ranging from 2 to 24 m s^{-1}. These groups were selected for the following reasons. First, the radiative fluxes are affected by the season, and it is therefore essential to make the model runs in both the presence and the absence of solar radiation. Second, the presence of clouds affects the relative importance of the turbulent and radiative fluxes.

3.2. Spatial distributions in the ABL of the steady-state results

The following results refer to ice-covered grids (21–92) unless stated otherwise. In a steady state, the heat budget of the ABL was governed by a balance between the horizontal advection and vertical diffusion. The other terms in Equation (1) were of minor importance. The horizontally averaged near-surface air temperature and wind speed are summarized in Table 2. First we compare the air temperature among the four groups of simulations (Fig. 2).

Table 2. Horizontally averaged 2 m air temperature (T_{air}, in $^\circ$C), snow surface temperature (T_s), snow/ice temperatures at the indicated depths, 10 m wind speed (V, in m s^{-1}), sensible- (Q_h) and latent- (Q_{le}) heat fluxes, and the net shortwave and longwave radiative fluxes (net SWR and net LWR, respectively). All fluxes are in W m^{-2} and positive towards the surface. The upper number in each block is the value from a model run with $G = 4$ m s^{-1}, and the lower number that from a model run with $G = 20$ m s^{-1}

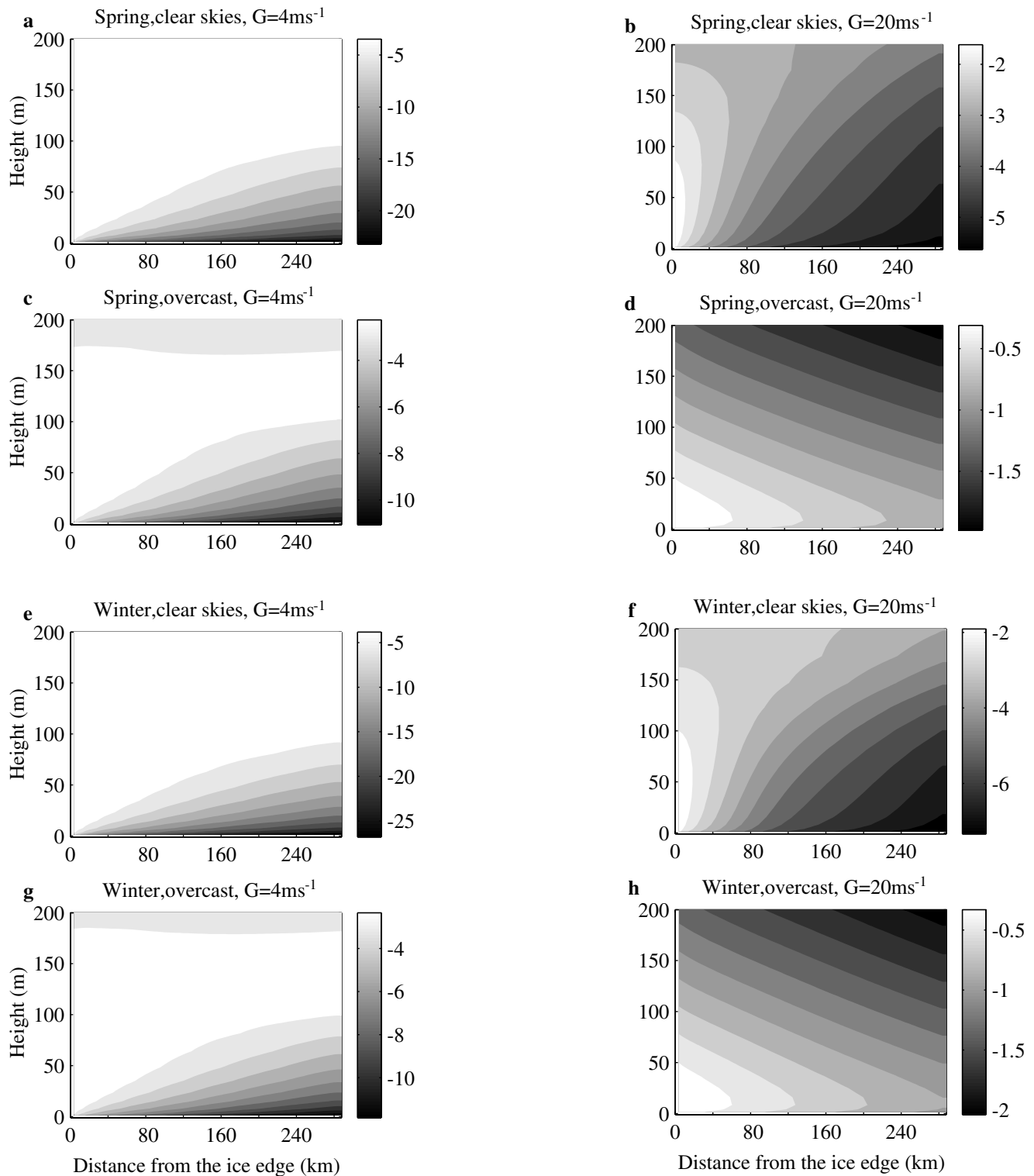| | Spring | | Winter | |
	Clear	Overcast	Clear	Overcast
T_{air} (2 m)	−16.5	−7.7	−19.1	−8.3
	−4.4	−0.5	−5.5	−0.6
T_s	−25.7	−10.2	−29.7	−10.9
	−6.9	−1.4	−8.1	−1.5
T (−0.05 m)	−23.2	−10	−27.5	−10.9
	−6.9	−2.3	−8.2	−2.3
T (−0.2 m)	−16.9	−9.9	−19	−10.2
	−8	−5.6	−8.7	−5.7
T (−1 m)	−10	−7.8	−10.4	−7.9
	−7.2	−6.5	−7.3	−6.5
V (10 m)	3.6	3.4	3.6	3.4
	10.4	11.6	10.3	11.6
Q_h	15	7	16	7
	50	19	51	19
Q_{le}	3	4	3	4
	−11	−4	13	−4
Net SWR	20	10	0	0
Net LWR	−40	−12	−35	−11
	−64	−9	−63	−9

427

Fig. 2. Cross-sections of the air temperature (in °C) in our eight basic scenarios after 10 model days. Note the different grey scales in the various subplots.

For a low geostrophic wind speed G of $4 \, \text{m s}^{-1}$, a cold, shallow internal boundary layer (IBL) develops over the ice. The differences in air temperature between the four groups are minor at heights above 100 m, where the air-mass modification from its state at the ice edge is <1 K, and the air temperature is therefore horizontally almost homogeneous. Close to the surface (at a height of 2 m) the decrease in the air temperature exceeds 18 K in clear-sky conditions (Fig. 2a and e). The cases with overcast skies are warmer ones and do not differ much from each other (Fig. 2c and g). The cooling over the 280 km fetch over the ice reaches 8–10 K in these cases. The smaller air-mass modification is

due to the reduced longwave cooling, leading to higher snow-surface temperatures.

For a high geostrophic wind speed of $20 \, \text{m s}^{-1}$, in clear-sky conditions (Fig. 2b and f) the IBL grows downwind much faster than in the case of $G = 4 \, \text{m s}^{-1}$. Under overcast skies (Fig. 2d and h) the temperature inversion layer remains very shallow (10–15 m), and above it the stratification is close to neutral. The air-mass modification is smaller but extends to higher levels than with $G = 4 \, \text{m s}^{-1}$. If we define the air mass to be modified when the horizontal change in the air temperature exceeds 0.5 K, the modification extends to heights of 180–200 m. The horizontally averaged 2 m air
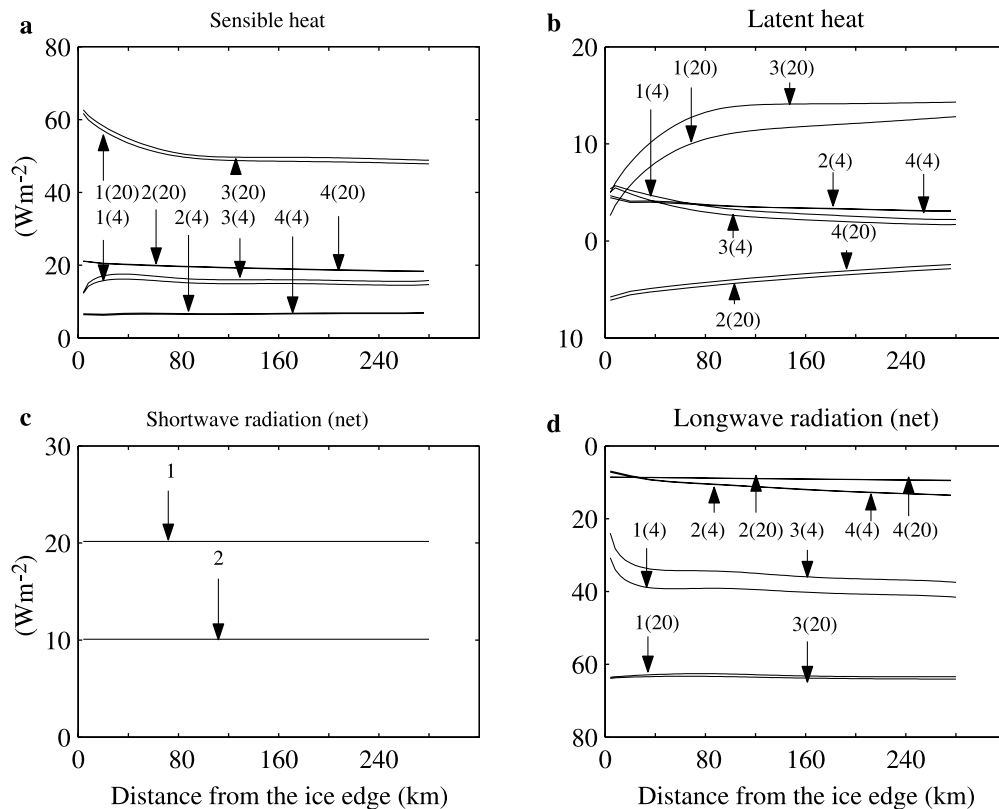
428

Fig. 3. Horizontal distributions of the surface fluxes of (a) sensible heat, (b) latent heat, (c) net shortwave radiation and (d) net longwave radiation after 10 model days. The four groups of the model runs are marked with the numbers: 1 (spring clear skies); 2 (spring overcast skies); 3 (winter clear skies); and 4 (winter overcast skies). The numbers in parentheses give the geostrophic wind speed in $m\,s^{-1}$. The differences in the results of the turbulent heat fluxes and the longwave radiation flux between spring overcast and winter overcast are very small, especially for $G = 4\,m\,s^{-1}$, so the two lines 2(4) and 4(4) merge.

temperature is 7–14 K higher than with $G = 4\,\mathrm{m\,s^{-1}}$, and now varies by 5 K between the four groups, the overcast cases being the warmer ones. The vertical air-temperature gradient at $x = 100\,\mathrm{km}$, $z = 0$–$100\,\mathrm{m}$, is now $1\,\mathrm{K}\,(100\,\mathrm{m})^{-1}$ in the clear-sky cases, while it was much larger, 6–$17\,\mathrm{K}\,(100\,\mathrm{m})^{-1}$, in the cases with $G = 4\,\mathrm{m\,s^{-1}}$. This is related to the more effective mixing due to a stronger wind.

Considering the effect of wind speed on the air-mass modification, we may note the following aspects. A stronger wind

(1) yields larger turbulent fluxes,

(2) allows less time for the air mass to be modified over a certain fetch over the ice, and

(3) yields a stronger growth of IBL, with the heat loss distributed into a larger air mass.

The combined effect of aspects (1) and (3) makes the air temperature at heights $>150\,\mathrm{m}$ decrease more with increasing wind speed. Aspects (2) and (3) have a dominating effect on the air temperatures close to the surface: in all the four groups considered, the 2 m air temperature decreases more with a lighter wind (Table 2). Hence, with $G = 20\,\mathrm{m\,s^{-1}}$, the horizontally averaged 2 m air temperature is higher than with $G = 4\,\mathrm{m\,s^{-1}}$. The difference is smallest (7.2–7.7 K) in the overcast cases, in which the snow surface temperature is higher.

Next we consider the effect of cloud cover on the various cases. In the following, the terms "colder" and "warmer" refer to the 2 m air temperatures, which have the most direct effect on the ice thermodynamics. We see from Table 2 that in spring compared to the clear-sky conditions the cloud cover makes the horizontally averaged air temperature 8.8 K ($G = 4\,\mathrm{m\,s^{-1}}$) and 3.9 K ($G = 20\,\mathrm{m\,s^{-1}}$) warmer, while in winter the

effect is 10.8 K ($G = 4\,\mathrm{m\,s^{-1}}$) and 4.9 K ($G = 20\,\mathrm{m\,s^{-1}}$). In spring the cloud cover also reduces the downward solar radiation, and it is therefore natural that the warming effect is larger in winter. It is, however, interesting that the cloud effect depends much more on the wind speed than on the season (when the latter only ranges from December to March). Stronger winds also make the surface warmer under clear skies, and therefore the cloud effect cannot be as large as with lighter winds. Looking at the snow surface temperature, similar but even larger effects can be seen (Table 2).

The seasonal effect on the 2 m air temperature remains low, because the diurnal average net solar radiation over a strongly reflecting snow surface is only 10–$20\,\mathrm{W\,m^{-2}}$ at $70°\mathrm{N}$ on 21 March. In fact, both the surface and 2 m air temperatures depend more on the wind speed than on the season. The cloud-cover effect is stronger than the seasonal effect but weaker than the wind effect (Table 2).

The boundary-layer wind speed naturally depends on the geostrophic forcing. The stronger the geostrophic wind speed, the thicker is the boundary layer. Accordingly, with $G = 4\,\mathrm{m\,s^{-1}}$ the 10 m wind speed is 85–90% of G, while it is only 52–58% with $G = 20\,\mathrm{m\,s^{-1}}$ (Table 2). In general, the wind field did not show large differences between the four groups.

3.3. Spatial distributions in the ice and snow of the steady-state results

First we look at the horizontal distributions of the surface fluxes, which couple the air and the snow surface. The results for the four simulation groups with $G = 4$ and $20\,\mathrm{m\,s^{-1}}$ are shown in Figure 3. The sensible-heat flux (Q_h) depends above all on the cloud cover and the wind speed
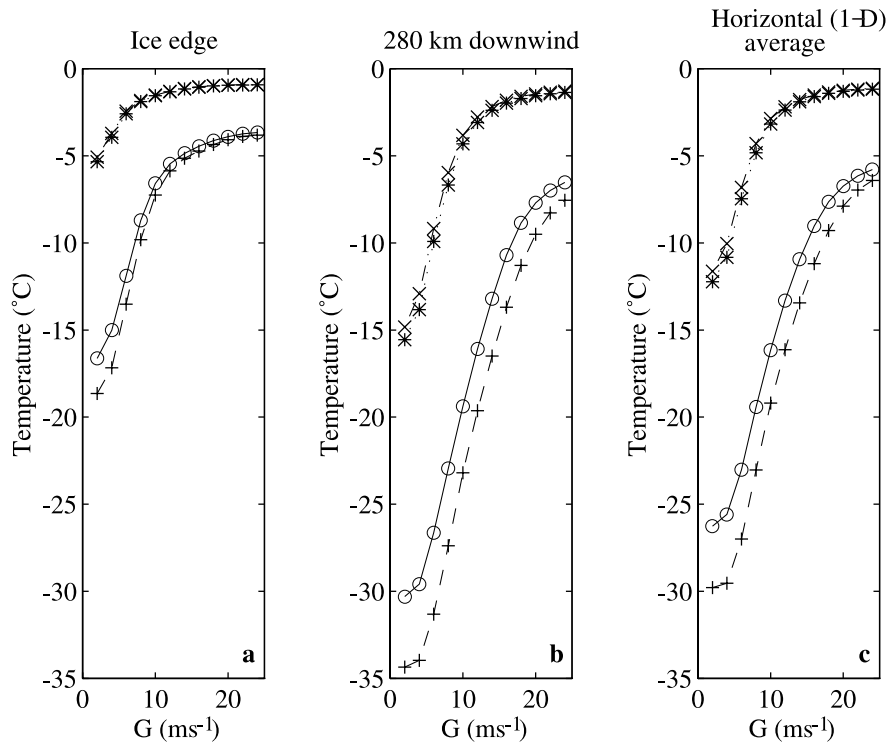
Fig. 4. Modelled snow surface temperature as a function of the geostrophic wind speed after 10 model days (a) at the upwind edge of the sea ice, (b) at the downwind edge after a fetch of 280 km, and (c) as a horizontal average over the sea ice. Different symbols indicate the four groups of the model runs: spring clear skies (○); spring overcast skies (×); winter clear skies (+); and winter overcast skies (∗).

(Fig. 3a). Under clear-sky conditions with $G = 20\,\mathrm{m\,s^{-1}}$, the surface receives $50-60\,\mathrm{W\,m^{-2}}$ via the sensible-heat flux, which balances most of the longwave cooling (Fig. 3d). Under overcast skies Q_h is $5-20\,\mathrm{W\,m^{-2}}$, as it is also under clear skies with a weak G of $4\,\mathrm{m\,s^{-1}}$. In this latter case Q_h first increases with fetch, while with a strong wind it decreases with fetch. In both cases, the air temperature decreases with fetch, tending to decrease Q_h, but just after the ice edge there is a local minimum in the near-surface wind speed, caused by the increased thermal stratification and surface roughness. With a light geostrophic wind, this dominates over the air-temperature modification.

The latent-heat flux Q_le has a smaller magnitude than Q_h but it varies relatively more. The requirements for a large downward Q_le are a strong wind and cold snow surface temperature which are met downwind from the ice edge. Due to the warm-air advection, Q_le is usually directed towards the surface, indicating condensation. It is strongest under clear skies, because the snow surface temperature is lower, although the relative humidity at the model inflow boundary is lower for clear than for overcast skies (70% and 100%, respectively). Evaporation takes place only with overcast skies and a strong wind. These correspond to the cases with the highest snow surface temperature (see Table 2). In the clear-sky cases, the fetch dependence is opposite to that for Q_h. Now, with high G, the condensation increases with fetch, because the surface becomes colder (Fig. 2b and f). At low G, the snow surface temperature is less affected, and the condensation slightly decreases with fetch because the near-surface air becomes drier with fetch.

The net shortwave radiation is constant with fetch and depends only on the cloud cover (Fig. 3c). The net longwave radiation is close to zero in the overcast cases, but negative under clear skies, in particular with strong winds. A strong wind increases both the surface and the air temperature, but

the effect on the snow surface temperature is larger (Table 2), and therefore the longwave radiation emitted from the surface increases more.

Figure 4 shows the modelled snow surface temperature vs the geostrophic wind for the four simulation groups. To depict the spatial variation, we plotted the snow surface temperature at the ice edge (gridpoint 21) and at the downwind edge of the model domain (gridpoint 92), as well as the horizontal average over the entire ice-covered model domain. The snow surface temperature near the ice edge is much higher than its initial low value ($-30°\mathrm{C}$), but it gradually decreases downwind of the ice edge. The total decrease over the 280 km fetch is $10-16\,\mathrm{K}$ with a weak G, and $0.5-3.5\,\mathrm{K}$ with a strong G (Fig. 4a and b). Considering the snow surface temperature at a fixed location, it increases exponentially with increasing G up to $G \approx 7-10\,\mathrm{m\,s^{-1}}$, but after that the increase is slower. The effect of G on the horizontally averaged snow surface temperature varies from $11\,\mathrm{K}$ in the overcast cases to $20-24\,\mathrm{K}$ in the clear-sky cases. The snow surface temperature difference among the four simulation groups increases with increasing distance from the ice edge.

The (x, z) cross-sections of the ice and snow temperatures after the 10 day long simulations for the four groups with $G = 4$ and $20\,\mathrm{m\,s^{-1}}$ are shown in Figure 5, and the horizontally averaged temperatures at selected depths are given in Table 2. In general, there is a vertical temperature gradient, indicating an upward heat flux through the ice and snow, but the warm-air mass has, in certain cases, heated the uppermost snow and ice layers so much that the temperature gradient has reversed. In the model runs with a large G and overcast skies, a horizontally homogeneous warm ice/snow layer is generated in the uppermost layers of the whole ice-covered model domain (Fig. 5d and h). This indicates a horizontally consistent downward conductive heat flux. Below this layer there is, however, an almost iso-
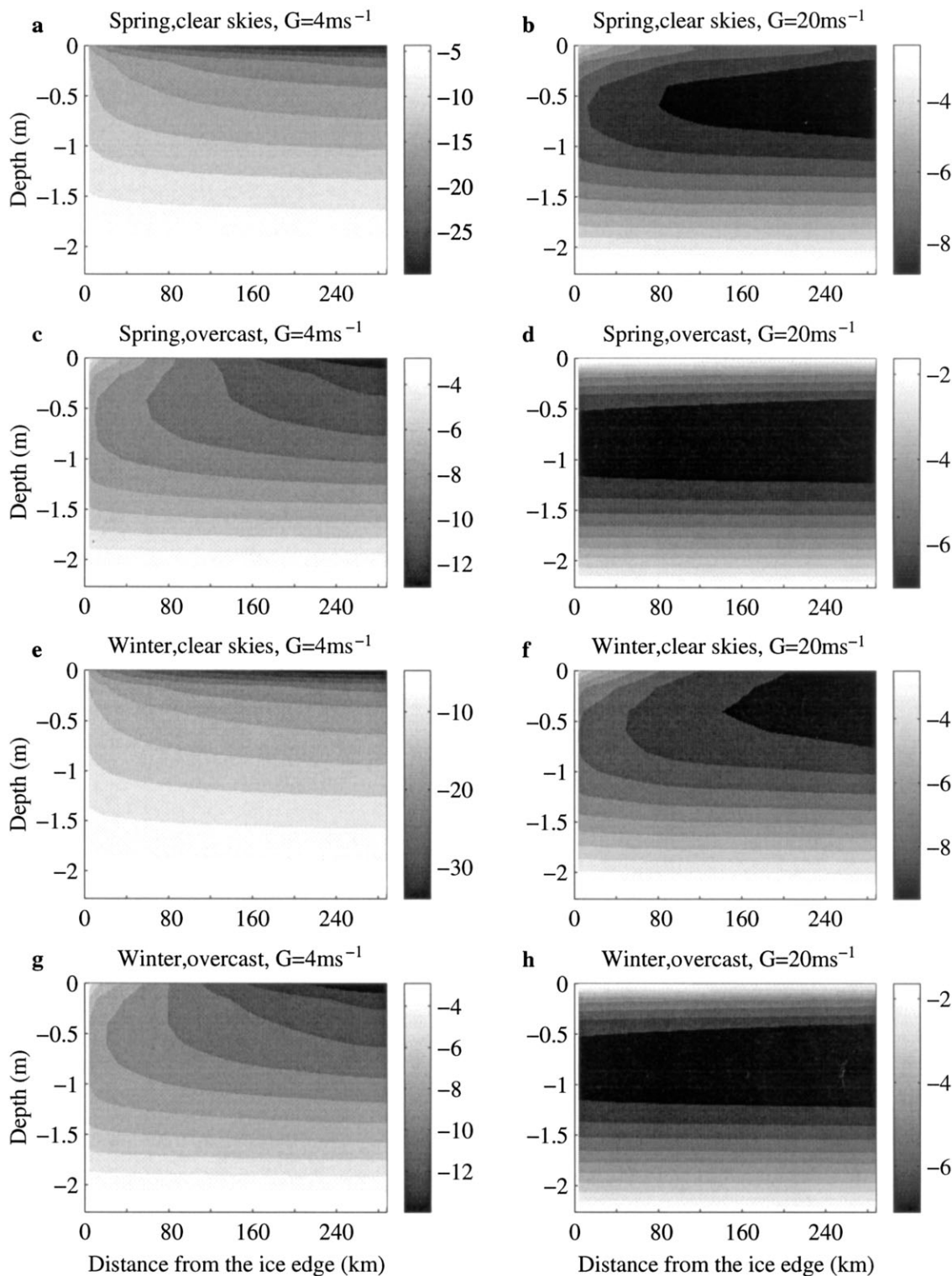
Fig. 5. *Cross-sections of the snow and ice temperatures (in °C) in our eight basic simulations. Note the different greyscales in the various subplots.*

thermal layer 0.8–1.0 m thick. In clear-sky conditions, the isothermal layer exists only with $G = 20\,m\,s^{-1}$, and in overcast conditions with $G = 4\,m\,s^{-1}$ it only occupies part of the model domain. Under clear skies, the heat loss via the strongly negative net longwave radiation is larger, and a strong wind is required to provide a sensible-heat flux large enough to make the uppermost snow and ice layers warmer than the lower layers. Under overcast skies, even a light wind is enough to generate a downward heat flux within some 80–100 km of the ice edge.

If we compare the cases for clear skies and overcast conditions for the same magnitude of G, the modelled in-ice temperatures are much higher for overcast-sky conditions, especially for the winter model runs. This is due to the effect of downward longwave radiation on the surface heat balance. In spring overcast conditions, the contribution of radiation to the surface heat balance also depends much more on the longwave than the shortwave flux. In the uppermost layers, the horizontal gradients of ice and snow temperatures are largest for the winter model runs with clear-sky conditions and a small G (Fig. 5e). In such conditions the effect of the warm-air advection reaches only the shortest fetches due to the compensating effect of the strong radiative cooling of the surface.

431

3.4. Relevance of the coupling and advection in steady-state simulations

The model runs presented in sections 3.2 and 3.3 are referred to as reference runs. To study the importance of the model coupling and the warm-air advection, we made the following control runs:

(a) Modelling of the ABL with the snow surface temperature fixed at its initial value of $-30°$C.

(b) Modelling of the ice and snow with a prescribed near-surface atmosphere. Accordingly, the ice model was forced at each gridpoint by the inflow properties of the marine air mass: $T_{air}(2m) = -1°$C, and $Rh(2m) = 70\%$ in clear-sky runs and 100% in overcast runs. For $V(2m)$ we used the steady-state results (dependent on G) of the coupled runs.

(c) Modelling of the coupled system without horizontal advection. The air–ice coupling is accordingly modelled in the form of one-dimensional exchange, and therefore the near-surface air temperature decreases from its initial value of $-1°$C, and the snow surface temperature may either increase or decrease from the initial $-30°$C.

(a), (b) and (c) each included eight model runs with $G = 4$ and $20\,\text{m s}^{-1}$ in the conditions shown in Table 1.

The results of the control runs are summarized in Table 3, where we show the heat gain of the ice and snow via the surface (ΔQ_{ice}) and that of the ABL (ΔQ_{air}). ΔQ_{ice} results from the time-integrated effect of the turbulent and radiative surface fluxes. The radiative fluxes partly penetrate through the ABL, and therefore ΔQ_{air} and ΔQ_{ice} do not balance each other. Because of the warm advection, the heat content of the ABL at a fixed location does not decrease as ΔQ_{air} would indicate.

In the reference runs, ΔQ_{air} mostly depends on the wind speed and cloud cover, and its absolute magnitude slightly decreases with distance from the ice edge (Table 3). In the runs with a fixed T_s ((a) runs), with $G = 4\,\text{m s}^{-1}$, $-\Delta Q_{air}$ is on average 1.5 times as large as in the reference run, while the ratio is 5.4 with $G = 20\,\text{m s}^{-1}$. Hence, from the point of view of the ABL modelling, the coupling is most important when the wind is strong. This is because the snow surface temperature increases due to the large sensible-heat flux. With $G = 20\,\text{m s}^{-1}$, the coupling makes the horizontally averaged T_{air} (2 m) warmer by 18 K (clear skies) to 22 K (overcast skies). In the clear-sky simulations with $G = 4\,\text{m s}^{-1}$, the turbulent fluxes are small, and the differences in $T_{air}(2\,\text{m})$ are within 2 K. With a fixed T_s the air mass cools faster with fetch, and $-\Delta Q_{air}$ decreases downwind more strongly than in the reference run (Table 3).

In the reference runs, ΔQ_{ice} is positive in all cases except during low winds under winter clear skies (Table 3), when the heat gain is not enough to balance the heat loss via longwave radiation. With the ABL fixed in the (b) runs, ΔQ_{ice} increases, and the increase is largest far from the ice edge, where the air mass is coldest in the reference runs. The increase is larger for light than for strong winds (see, e.g., $x = 100$ km for winter overcast skies in Table 3). This is opposite to the behaviour of ΔQ_{air}, and results from the fact that with a light wind the marine air mass cools more during a certain fetch over the ice. If this cooling is not modelled, the horizontally averaged snow surface temperature may even become 25 K too warm (under winter clear skies). Closer to the ice edge the errors are smaller but can still be as large as 15 K (winter clear skies) 10 km downwind of the ice edge. This has strong implications even if the air–surface coupling is modelled; errors of such a magnitude may occur in regional-scale models using grid lengths of the order of 20 km.

In the coupled runs without advection ((c) runs), the ABL heat loss was always smaller than in the reference runs (Table 3). This was because the air temperature decreased rapidly

Table 3. *The heat gain of the ABL (ΔQ_{air}, in $J\,m^{-2}$) and the ice and snow (ΔQ_{ice}) in 10 days for the coupled, uncoupled (fixed air or snow surface temperatures) and no-advection simulations (see the text for the description of runs (a–c)). The upper and lower numbers in each block refer to the model run with $G = 4$ and $20\,m\,s^{-1}$, respectively. The calculations are made for locations 10 and 100 km downwind of the ice edge*

	$\Delta Q_{air} \times 10^7$							
	X = 10 km				X = 100 km			
	Spring clear sky	*Spring overcast*	*Winter clear sky*	*Winter overcast*	*Spring clear sky*	*Spring overcast*	*Winter clear sky*	*Winter overcast*
Coupled = reference run	−1.75 −5.28	−0.94 −1.59	−1.83 −5.89	−0.96 −1.64	−1.49 −5.03	−0.91 −1.61	−1.58 −5.57	−0.93 −1.66
Fixed T_s = run (a)	−2.08 −16.37	−2.08 −16.37	−2.08 −16.37	−2.08 −16.37	−1.58 −11.11	−1.58 −11.11	−1.58 −11.11	−1.58 −11.11
No advection = run (c)	−0.77 −2.06	−0.57 −1.4	−0.8 −2.18	−0.58 −1.43	−0.77 −2.05	−0.57 −1.4	−0.8 −2.12	−0.58 −1.43

	$\Delta Q_{ice} \times 10^7$							
	X = 10 km				X = 100 km			
	Spring clear sky	*Spring overcast*	*Winter clear sky*	*Winter overcast*	*Spring clear sky*	*Spring overcast*	*Winter clear sky*	*Winter overcast*
Coupled = reference run	0.46 1.57	0.83 1.25	−0.64 0.59	0.47 0.89	0.17 1.35	0.46 1.21	−1.32 0.34	0.9 0.87
Fixed T_a = run (b)	1.33 1.58	1.26 1.3	0.37 0.66	0.9 0.95	1.33 1.57	1.26 1.3	0.37 0.66	0.91 0.95
No advection = run (c)	−1.2 −0.48	−0.63 −0.22	−2.24 −1.38	−1.02 −0.41	−1.2 −0.47	−0.62 −0.21	−2.24 −1.36	−1.02 −0.41

and could not maintain a large downward sensible-heat flux and ΔQ_{ice} was negative in all (c) runs. Had we included the oceanic heat flux (here $10\,W\,m^{-2}$) and the release of latent heat due to bottom freezing (here up to 0.025 m) in the definition of ΔQ_{ice}, the values would have always been positive. These negative values resulted because in the case of no warm advection the air temperature cooled rapidly and therefore the snow surface temperature always remained colder than the ice bottom temperature. Hence, heat was continuously conducted through the ice and emitted from the surface in the form of longwave radiation. The difference in ΔQ_{air} between the (c) runs and the reference runs was largest during strong winds under clear skies, indicating those conditions in which the warm-air advection was most important for the ABL. Now the situation was the same from the point of view of the ice and snow since ΔQ_{ice} also differed most between the (c) runs and the reference runs during strong winds under clear skies. This was due to a combination of effects: strong winds made ΔQ_{ice} and $-\Delta Q_{air}$ large in the reference runs, while in the (c) runs the surface heat loss via longwave radiation was naturally larger under clear than overcast skies, reducing ΔQ_{ice} and indirectly ΔQ_{air}.

From the point of view of uncoupled atmosphere and sea-ice models, it is important to understand the fetch over which spatial gradients occur in the marginal ice zone (MIZ) during warm-air advection. One possibility to define such a characteristic fetch is a criterion for the snow surface temperature gradient dT_s/dx. We found the value $0.1\,K\,km^{-1}$ as a relevant limit: $|dT_s/dx|$ had maximum values of the order of $1\,K\,km^{-1}$, but, independent of the cloud cover, season and wind speed, far enough from the ice edge $|dT_s/dx|$ always decreased below $0.1\,K\,km^{-1}$. According to this criterion, the characteristic fetch (F) for warm-air advection depends on the geostrophic wind speed as follows:

$$F = X - 1.3G\,, \qquad (4)$$

where $X \approx 40\,km$ in clear-sky conditions and $X \approx 18\,km$ in overcast conditions, and G is in $m\,s^{-1}$. In overcast conditions, for $G \geq 14\,m\,s^{-1}$, $|dT_s/dx|$ was everywhere smaller than the criterion, and there was no characteristic fetch representing the transition zone for the snow surface temperature (Fig. 5d and h). In such conditions, the effects of warm-air advection reach fetches larger than those we could realistically simulate using a mesoscale model (which assumes, for example, a horizontally uniform pressure gradient). A different definition for the characteristic fetch should be applied to represent the fetch over which the warm-air advection has implications (cf. Andreas and Makshtas, 1985).

3.5. Temporal evolution in the snow and ice

The model runs are made for a 10 day period to allow the coupled air–ice system to reach a steady state. Such a long period was necessary because of the large thermal inertia of ice and snow compared to that of the ABL. In reality, however, the meteorological situation seldom remains unchanged so long that a steady state is reached throughout the entire depth of a thick sea-ice cover. To understand the impacts of a shorter warm-air advection situation, we look at the temporal evolution of the snow and ice thermodynamics.

The temporal evolution of the vertical temperature regime depends on the location from the ice edge. We first concentrate on a fixed location 52 km downwind of the ice edge (Fig. 6). Under spring clear skies, the oscillation of temperature of the upper part of the snow and ice reflects the

diurnal variation of solar radiation (Fig. 6a and b). With a light wind, the diurnal variation of temperature reaches a depth of 0.3–0.4 m, but is larger in the top 0.2 m. During winter clear skies with a small G (Fig. 6e), the surface heat gain is minimized. Accordingly, the snow surface temperature is not much affected by the warm advection, and thus the inherent upward conductive heat flux in the snow and ice does not change in time. The snow and ice temperatures therefore remain almost unchanged.

Except for the coldest cases (Fig. 6a and e), the other cases show a qualitatively similar evolution of the temperature profile. With a light wind (Fig. 6c and g), the depth of the local temperature minimum first increases rapidly, but after approximately 20 hours it reaches a stationary position at about 0.4 m. This is due to the competing effects of the conductive heat fluxes originating from the surface and the ice bottom. That from the surface starts to be effective after the 6 hour initialization period, and then it gradually makes the near-surface layers warmer until a balance is reached. With a strong wind, the stationary depth for the temperature minimum is lower, 0.6–0.8 m, and is accordingly reached later, after some 100 hours.

The above results were for a location 52 km downwind of the ice edge. Further downwind (not shown in figures), the temporal evolution of the vertical temperature regime was qualitatively similar, but due to the smaller surface heat flux the temperatures were lower and the evolution slower.

To understand the mechanisms for the above-mentioned features, we look at the heat-conduction equation (3). Under polar winter conditions, the last term in Equation (3) can be ignored. The heat-conduction equation of snow can be replaced by Fick's diffusion law, i.e. the rate of increase of the internal energy (first term in Equation (3)) balances the convergence of the vertical heat flux (second term). In spring conditions, particularly under clear skies, the last term in Equation (3) acts as an internal heating source item and modifies the diurnal ice/snow temperature wave. We estimated the magnitude of each term in Equation (3) in spring clear-sky conditions with $G = 4\,m\,s^{-1}$ for a depth of 0.1 m in the snow. During the fifth simulation day, the diurnal mean $(\rho c)_{sn}(\partial T_{sn}/\partial t)$ was small ($2\,W\,m^{-3}$). The diurnal mean solar heating term $-\partial q_{sn}/\partial z_i = \kappa(1-\alpha)Q_s e^{-\kappa z_i}$ was $65\,W\,m^{-3}$, which was practically balanced by the vertical flux divergence term with a mean value of $-63\,W\,m^{-3}$. During the daylight period (0600–1800 h), the mean $(\rho c)_{sn}(\partial T_{sn}/\partial t)$ was much larger ($30\,W\,m^{-3}$), but the solar heating term ($129\,W\,m^{-3}$) was still mostly balanced by the vertical flux divergence ($-99\,W\,m^{-3}$).

The conductive heat flux in the uppermost layers may change its direction at a certain horizontal location downwind of the ice edge. This is, however, only possible when the surface heat flux is large enough. Further downwind from the ice edge, the air mass is cooler, and the heat flux through the ice and snow turns upwards, as it would be without the warm-air advection. The horizontal location of the change in the direction of the conductive heat flux depends on the time development of the warm-air advection, the heat conduction in the snow and ice, the cloud cover and the solar radiation.

We analyzed the diurnal mean conductive heat flux between the surface and a depth of 0.1 m for the whole ice-covered model domain. The selection of 0.1 m is somewhat arbitrary but is quite commonly used as the thickness of the uppermost layer (directly related to the surface heat balance) in thermodynamic sea-ice models (Maykut and
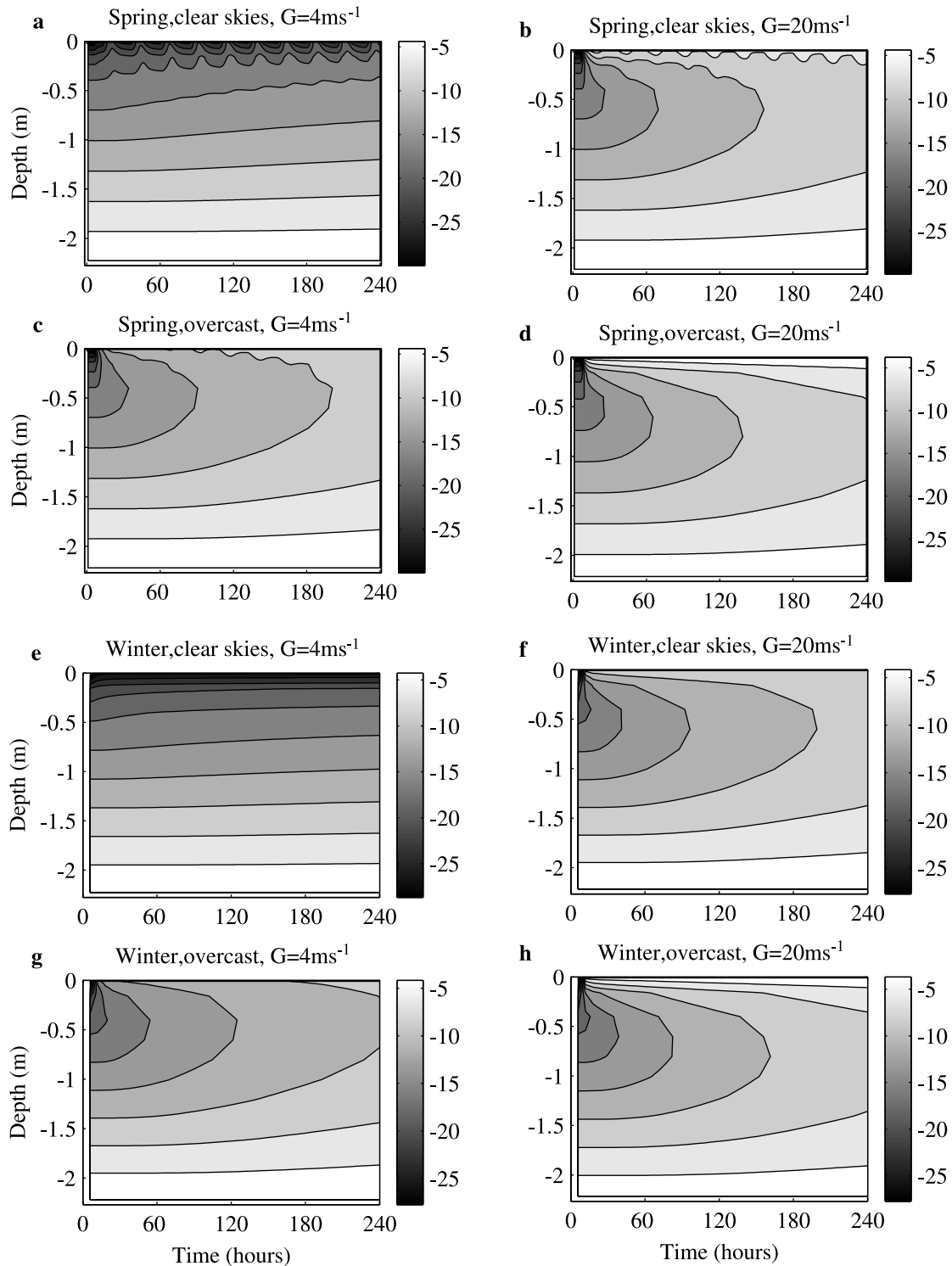
Fig. 6. Time series of snow and ice temperatures (in °C) 52 km downwind of the ice edge in our eight basic scenarios.

Untersteiner, l97l; Ebert and Curry, l993). Under winter clear skies (Fig. 7a), the location where the conductive heat flux changes its direction depends strongly on the wind speed, the distance from the ice edge increasing as the wind increases. In overcast-sky conditions (Fig. 7b), the surface is warmer, and therefore even a weaker wind can create a region of downward conductive heat flux. With $G = 4 \, \mathrm{m \, s^{-1}}$ the width of the region decreases from 200 km on the second day to 90 km on the tenth day. With a stronger wind, the downward flux prevails over the whole ice-covered model domain (and there are accordingly no points for stronger winds in Figure 7b). In every case, the change in the flux direction does occur, however, at some larger depth: the depths after a l0 day model run are shown in Figure 5. Con-

centrating on the diurnal means, the results for spring (not shown) were practically the same as those for winter.

The downward flux gradually heats the snow and ice below the surface, decreasing the vertical temperature gradient. After a sufficiently long time, a temperature profile monotonously decreasing upwards is reached, indicating that at a fixed location the near-surface downward heat flux can change to an upward flux (Fig. 8a and b). Hence, the horizontal region where this downward flux occurs reaches its maximum width within a few hours after the 6 hour initialization period. (In situ, it would reach it within a few hours after the arrival of the warm air mass.) Therefore, the horizontal region of the downward flux decreases, as we see from Figure 7a and b by comparing the values after 2, 5 and 10 days.

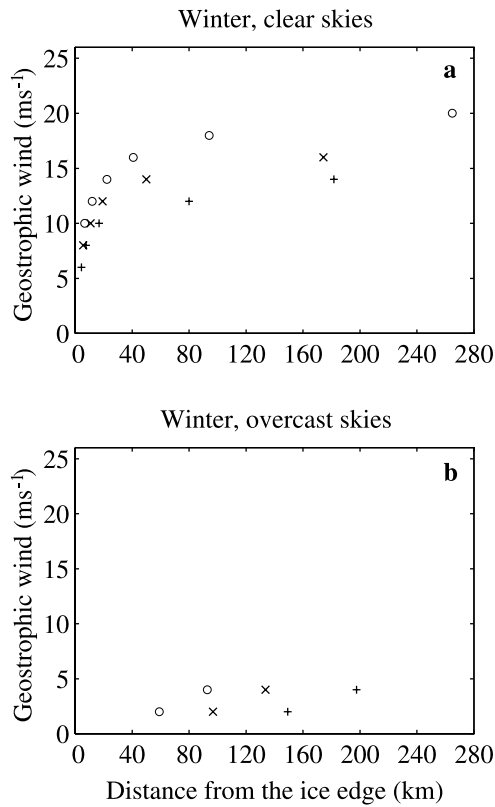## Winter, clear skies

Winter, overcast skies

Fig. 7. Modelled location of the reversed conductive heat flux in the uppermost 0.1 m of snow as a function of the geostrophic wind speed in winter (a) clear skies, and (b) overcast skies. The diurnal mean locations on the second (+), fifth (×), and tenth day (○) of the simulation are shown.
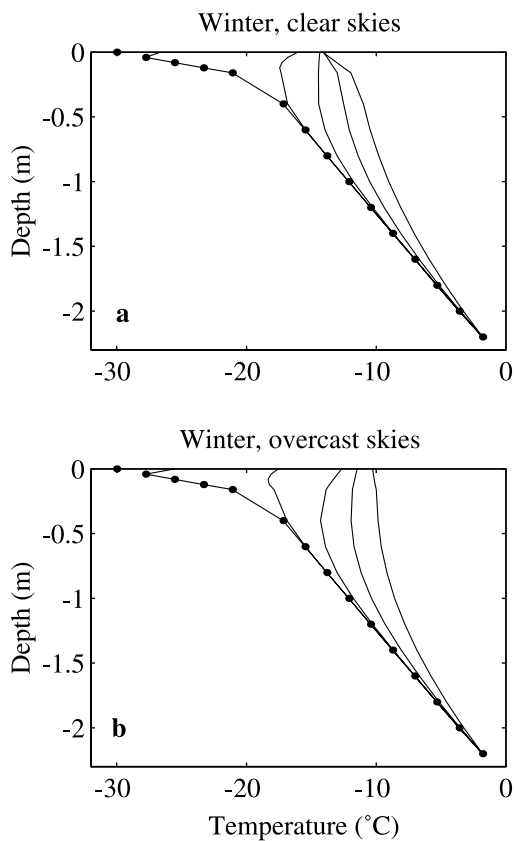
Winter, clear skies

Winter, overcast skies

Fig. 8. Vertical snow/ice temperature profiles: (a) 50 km downwind of the ice edge with $G = 12\,m\,s^{-1}$; (b) 100 km downwind with $G = 4\,m\,s^{-1}$. The dots indicate the initial profile, and the lines from left to right are the model output after 7 hours, 12 hours, second, fifth and tenth days.
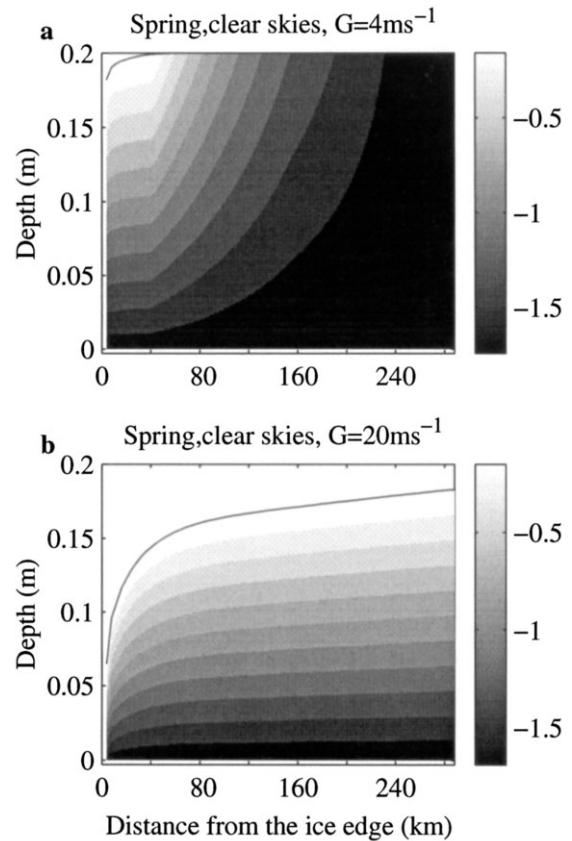
Spring, clear skies, G=4ms^{-1}

Spring, clear skies, G=20ms^{-1}

Fig. 9. Modelled cross-section of snow temperature (in °C) in a 30 hour model run with warm air ($T_a = +5°C$) advected over a snow surface with an initial $T_s = -2°C$. The surface evolution due to melting is taken into account. On the y axes, 0 gives the snow/ice interface.

With increasing wind speed the lifetime of a wide region of downward heat flux gets longer. For example, under clear skies (Fig. 7a), with $G = 6\,m\,s^{-1}$, on the second day a downward flux occupies a region 5 km wide, but on the fifth day the flux is already upward everywhere. With $G = 16\,m\,s^{-1}$, on the second day a downward flux prevails everywhere, and still on the tenth day it occupies a region 40 km wide.

3.6. Sensitivity tests

3.6.1. Initially warmer ice and snow
In the previous sections we have concentrated on initially very cold ice, which consequently effectively cools the ABL. To understand the effects of warm-air advection on ice thermodynamics in warmer conditions, we made new simulations with the initial snow surface temperature set to $-2°C$ and the inflow near-surface air temperature to $+5°C$. We confine our concentration to the spring equinox and overcast skies. The snow surface albedo is assumed to be 0.8, but it decreases to 0.7 if the surface starts to melt (Perovich, 1996). We focus our attention on the surface mass balance, and accordingly ignore the mass balance at the ice bottom. To prevent total snow melting, the model runs were made for a 30 hour period.

The cross-sections of the snow temperature are shown in Figure 9 (the ice temperature is now almost uniform and therefore not shown). Comparing to Figure 5a and b, we see major differences: with both $G = 4\,m\,s^{-1}$ and $G = 20\,m\,s^{-1}$ the temperature now decreases with depth, while in Figure 5a ($G = 4\,m\,s^{-1}$) it increased with depth. In Figure 5a ($G = 20\,m\,s^{-1}$) the snow temperature (uppermost 0.2 m) decreased with depth, but the horizontal gradient was large. Now the
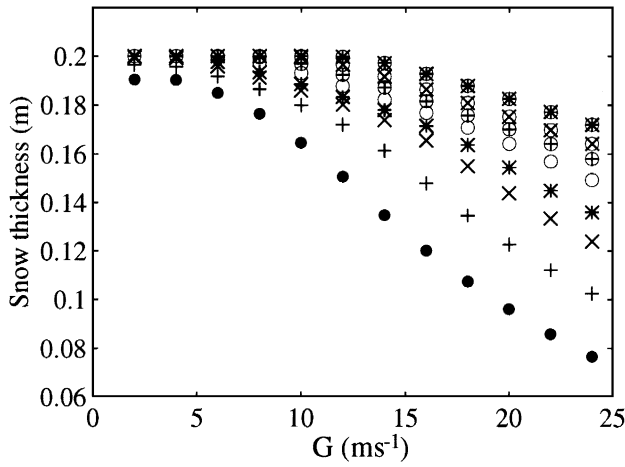
435

*Fig. 10. Modelled surface mass balance vs G at various locations. For each G the various symbols indicate the final snow thickness at 10 km (•), 20 km (+), 40 km (×), 60 km (*), 100 km (○), 150 km (⊕), 200 km (⊗) and 280 km (⋆) downwind of the ice edge.*

snow surface temperature is almost homogeneous with a high G, and with a low G the $|\mathrm{d}T_s/\mathrm{d}x|$ nowhere exceeds the limit $0.1\,\mathrm{K\,km}^{-1}$ (see section 3.4). The surface mass balance at selected locations is shown in Figure 10 as a function of G. For a weak wind, the surface melting was small and the horizontal differences in the mass balance were also small. For a high G, melting occurs throughout the model domain but strongly depends on the fetch.

3.6.2. Gradually increasing ice concentration and thickness
In all previous simulations we have set a step change from the open sea to a thick, compact ice cover. It is realistic for cases of long-lasting on-ice flows, in which the wind packs

the ice edge compact and the ice thickness increases due to rafting and ridging processes. However, usually in the marginal ice zone, and in on-ice flow cases of a shorter duration, the ice concentration and thickness gradually increase over tens of kilometres. We therefore made simulations analogous to those presented in section 3.1, but the ice concentration was set to increase linearly from 0 to 1 and the initial ice thickness (h_i) from 0 to 2 m under a distance of 60 km. The snow thickness was set as $\min(0.2h_i, 0.2\,\mathrm{m})$. In the model gridcells with a fractional ice cover, the grid-averaged surface fluxes were calculated applying the mosaic method (Vihma, 1995). The resulting temperature cross-sections are shown in Figure 11. Now we have a warm region close to the ice edge: in the thin ice the downward heat flux due to the warm-air advection together with the upward heat flux from the sea make the entire ice and snow cover warm. This is further enhanced by the upward heat flux from the open leads, which reduces the cooling of the air. In the fractured ice zone under clear skies with $G = 4\,\mathrm{m\,s}^{-1}$, the difference in the snow surface temperature from the simulations with a step change reaches 14 K (cf. Figs 5a and 11a).

4. CONCLUSIONS

We studied the advection of warm air over sea ice because its effects are in many respects more interesting than those of cold-air advection. During warm-air advection the air–ice turbulent heat flux has a direction opposite to the prevailing upward heat flux from the ocean through the ice. This results in a time- and fetch-dependent behaviour of the directionally varying conductive heat flux in the ice or snow.

We developed and applied a two-dimensional, coupled mesoscale atmosphere–sea-ice model to simulate this interaction. In fact, the thermodynamic ice model was one-
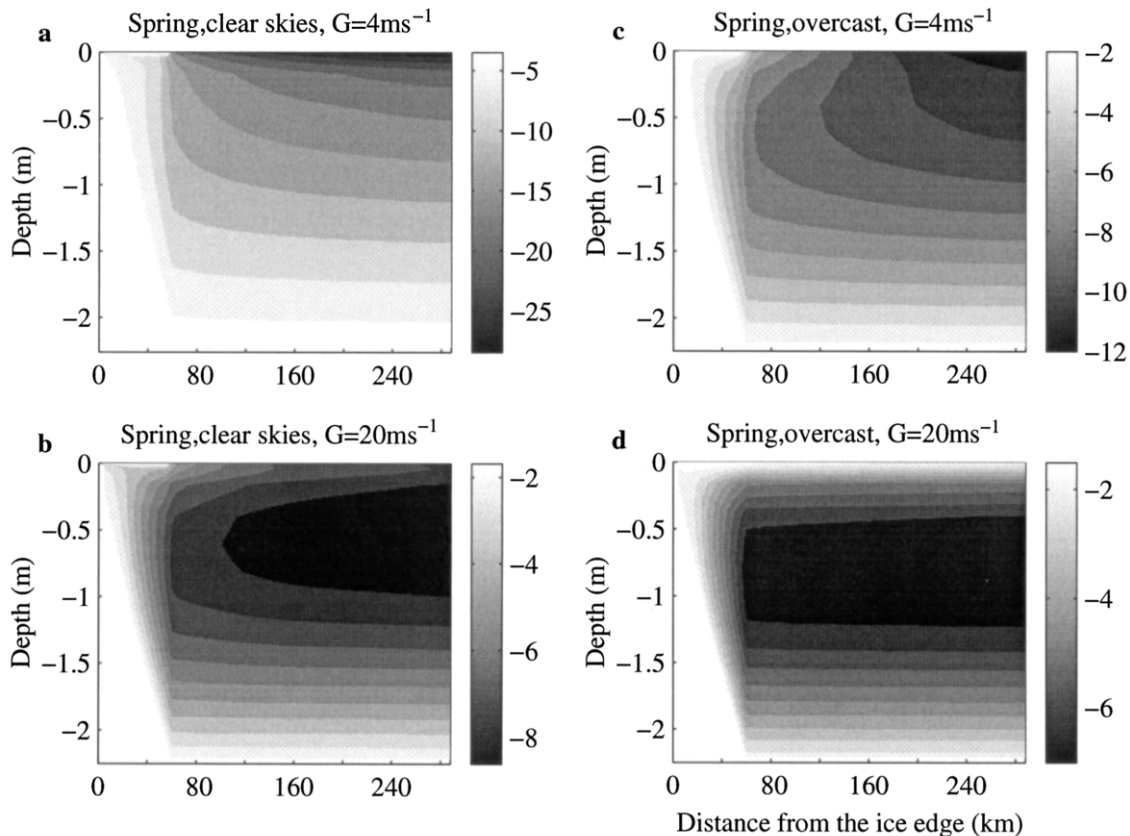

Fig. 11. The cross-sections of the snow and ice temperature (in °C) for model runs with a gradually increasing ice concentration and initial ice thickness. Note the different greyscales in the various subplots.

dimensional but coupled to the ABL model at each of the surface gridpoints. The horizontal heat conduction inside the ice and snow was accordingly ignored, but this did not affect the results, since the horizontal temperature gradients inside the ice and snow are only a small fraction of the vertical gradients.

The development of the stably stratified atmospheric boundary layer downwind of the ice edge depended above all on the wind speed and cloud cover. The wind speed had various kinds of effects: a strong wind (1) yields large turbulent fluxes, (2) allows less time for the air mass to be modified over a certain fetch, and (3) makes the boundary layer grow higher. Effects (1) and (3) together made the air temperatures over a height of 150 m decrease more with increasing wind speed. Effects (2) and (3) dominated for the near-surface temperatures, making them decrease less with increasing wind. The snow surface temperature depended most on the wind speed, then on the cloud cover, and least on the season. Except in the temporal variation in the diurnal period, the effect of the season was not particularly important in our model runs, for three reasons: the large surface albedo kept the net shortwave radiation small, the inflow properties of the marine air mass were kept constant (except in section 3.6.1) and we did not model a summer situation. We wanted to concentrate on seasons when a large difference between the air and snow surface temperature is realistically liable to occur.

Various effects compensating each other affected the spatial distribution of the turbulent surface fluxes, and their relative importance depended on the case chosen. Thus, the sensible- and latent-heat fluxes can either increase or decrease with fetch over the ice (Fig. 4). The dependence of the ice and snow temperature on the fetch was larger in conditions where the sensible-heat flux dominated (strong wind and clear skies; Fig. 5) than in conditions where the radiative fluxes dominated (light wind or clear skies). If the turbulent heat flux from air to snow was large enough to compensate the radiative cooling of the surface, a downward conductive heat flux was generated in the upper ice and snow layers. The stronger the surface heating, the wider was the region where this downward flux occurred. The effects of the warm-air advection in the upper snow and ice layers were most pronounced within a few hours after the beginning of the coupled simulation. After that the near-surface layers slowly returned to their undisturbed state of an upward conductive heat flux, seen as a reduction in the horizontal area where the downward flux occurred (Fig. 8).

We studied the importance of the modelling of the interactive coupling between the air and ice. From the point of view of modelling the atmospheric boundary layer, the coupling was most important when the wind was strong, because then the modification in the snow surface temperature was largest. From the point of view of modelling the snow and ice thermodynamics, the coupling was most important when the wind was weak, because then the modification in the air temperature was largest. In melting conditions the situation is, however, more complicated. The warm-air advection was most important, from the point of view of both ABL and the ice, during strong winds under clear skies. Without advection the ABL would have lost much less heat, while the ice and snow would have lost heat via the surface instead of gaining it (in the conditions of our study). We defined a characteristic fetch for warm-air advection as a fetch required for the snow surface temperature gradient to decrease below $0.1\,\mathrm{K\,km^{-1}}$.

This fetch depended on the cloud cover and wind speed according to Equation (4).

From the point of view of model applications it is also important to understand the very different time-scales of the thermal processes in the ABL, at the surface, and inside the ice and snow: approximately 10 days were required to reach a steady thermodynamic state in an ice cover 2 m thick. The time required depended on the case, and even after 10 days some evolution took place in certain cases (Fig. 6). Even quite significant qualitative changes took place on a scale of days, such as the evolution of the width of the region with a downward conductive heat flux. On the other hand, the snow surface temperature responded very quickly to the changes in the surface energy balance (Fig. 6a), due to the low heat conductivity of snow. The diurnal cycle only reached depths of the order of 0.2 m, and in this our model results are in agreement with the observations of Brümmer and others (1994).

The basic cases we modelled represented rather extreme, yet realistic, on-ice flow conditions with a marine air mass flowing over a surface initially almost 30 K colder. Such conditions are theoretically interesting, but also important for regional and large-scale modelling, because large errors may be generated both in such atmospheric models that use a prescribed snow surface temperature and in such thermodynamic ice models that use a prescribed atmospheric forcing. If the grid resolution is too coarse, errors are liable to occur over the ice-edge zone, even in coupled models. Close to the ice edge the ice thermodynamics may differ drastically from that in the inner sea-ice zone, and during warm-air advection it may take hundreds of kilometres of fetch before the near-surface air temperature has finally adjusted to be in balance with the ice surface, in particular if the wind is strong. This is in agreement with the observations of Andreas and Makshtas (1985) from the Weddell Sea.

The 2-D evolution of snow, ice and air temperatures naturally depends on the structure of the ice-edge zone. Our sensitivity studies suggest that when the ice concentration and thickness increase gradually over tens of kilometres, warm-air advection can make this zone much warmer than in the case of a step change between open water and a thick, compact sea-ice cover. Warm-air advection can be an important factor causing significant episodes of surface melting (Andreas and others, 1984). In our simulations the melting strongly depended on the wind speed and, if the wind was strong enough to cause significant melting, also on the fetch over the ice. These aspects, which we briefly addressed in the model sensitivity studies, deserve further research.

ACKNOWLEDGEMENTS

REFERENCES

Alestalo, M. and H. Savijärvi. l985. Mesoscale circulations in a hydrostatic model: coastal convergence and orographic lifting. *Tellus*, **37A**(2), 156–162.

Andreas, E. L. 1987. A theory for the scalar roughness and the scalar transfer coefficients over snow and sea ice. *Boundary-Layer Meteorol.*, **38**(1–2), 159–184.

Andreas, E. L. and A. P. Makshtas. l985. Energy exchange over Antarctic sea ice in the spring. *J. Geophys. Res.*, **90**(C4), 7199–7212.

Andreas, E. L., W. B. Tucker, III and S. F. Ackley. l984. Atmospheric boundary-layer modification, drag coefficient, and surface heat flux in the Antarctic marginal ice zone. *J. Geophys. Res.*, **89**(C4), 649–66l.

Bennett, T. J., Jr. l982. A coupled atmosphere–sea ice model study of the role of sea ice in climatic predictability. *J. Atmos. Sci.*, **39**(7), 1456–1465.

Bennett, T. J., Jr and K. Hunkins. l986. Atmospheric boundary layer modification in the marginal ice zone. *J. Geophys. Res.*, **91**(C11), 13,033–13,044.

Brümmer, B., B. Busack, H. Hoeber and G. Kruspe. l994. Boundary-layer observations over water and Arctic sea-ice during on-ice flow. *Boundary-Layer Meteorol.*, **68**(1–2), 75–108.

Cheng, B. l996. [The conservative difference scheme and numerical simulation of a one-dimensional thermodynamic sea ice model.] [*Marine Science Bulletin*], **15**(4), 8–15. (English transl. in Finnish Institute of Marine Research Contributions 5.) [In Chinese.]

Cheng, B. 2002. On the modelling of sea ice thermodynamics and air–ice coupling in the Bohai Sea and the Baltic Sea. (Ph.D. thesis, Finnish Institute of Marine Research, Helsinki; FIMR Contribution 5.)

Cheng, B. and J. Launiainen. l998. A one-dimensional thermodynamic air–ice–water model: technical and algorithm description report. *Meri*, **37**, 15–35.

Cheng, B., J. Launiainen, T. Vihma and J. Uotila. 200l. Modelling sea-ice thermodynamics in BALTEX-BASIS. *Ann. Glaciol.*, **33**, 243–247.

Ebert, E. E. and J. A. Curry. l993. An intermediate one-dimensional thermodynamic sea ice model for investigating ice–atmosphere interactions. *J. Geophys. Res.*, **98**(C6), 10,085–10,109.

Fairall, C.W. and R. Markson. l987. Mesoscale variations in surface stress, heat fluxes, and drag coefficient in the marginal ice zone during the l983 Marginal Ice Zone Experiment. *J. Geophys. Res.*, **92**(C7), 6921–6932.

Grenfell, T. C. and G. A. Maykut. l977. The optical properties of ice and snow in the Arctic Basin. *J. Glaciol.*, **18**(80), 445–463.

Holtslag, A. A. M. and H. A. R. de Bruin. l988. Applied modeling of the nighttime surface energy balance over land. *J. Appl. Meteorol.*, **27**(6), 689–704.

Jacobs, J. D. l978. Radiation climate of Broughton Island. *In* Barry, R. G. and J. D. Jacobs, *eds. Energy budget studies in relation to fast-ice breakup processes in Davis Strait: climatological overview.* Boulder, CO, University of Colorado. Institute of Arctic and Alpine Research, l05–120. (INSTAAR Occasional Paper 26.)

Joffre, S. M. l982. Momentum and heat transfers in the surface layer over a frozen sea. *Boundary-Layer Meteorol.*, **24**(2), 211–229.

Joffre, S. M. l988. Modelling the dry deposition velocity of highly soluble gases to the sea-surface. *Atmos. Environ.*, **22**(6), 1137–1146.

Kantha, L. H. and G. L. Mellor. l989. A numerical model of the atmospheric boundary layer over a marginal ice zone. *J. Geophys. Res.*, **94**(C4), 4959–4970.

Launiainen, J. and B. Cheng. l998. Modelling of ice thermodynamics in natural water bodies. *Cold Reg. Sci. Technol.*, **27**(3), 153–178.

Launiainen, J., C. Bin, J. Uotila and T. Vihma. 200l. Turbulent surface fluxes and air–ice coupling in Baltic Air–Sea–Ice Study (BASIS). *Ann. Glaciol.*, **33**, 237–242.

Long, P. E., W. A. Schaffer, J. E. Kemper and F. J. Hicks. l978. *The state of the Techniques Development Laboratory's boundary layer model May 24, 1977.* Silver Spring, MD, U.S. National Oceanic and Atmospheric Administration. (NOAA Tech. Mem. NSW TDL 66.)

Mahrer, Y. and R. A. Pielke. l978. A test of an upstream spline interpolation technique for the advective terms in a numerical mesoscale model. *Mon. Weather Rev.*, **106**(6), 818–830.

Maykut, G. A. l978. Energy exchange over young sea ice in the central Arctic. *J. Geophys. Res.*, **83**(C7), 3646–3658.

Maykut, G. A. and N. Untersteiner. l971. Some results from a time-dependent thermodynamic model of sea ice. *J. Geophys. Res.*, **76**(6), 1550–1575.

Overland, J. E. and P. M. Guest. l991. The Arctic snow and air temperature budget over sea ice during winter. *J. Geophys. Res.*, **96**(C3), 4651–4662.

Perovich, D. K. l996. The optical properties of sea ice. *CRREL Monogr.* 96-1.

Prata, A. J. l996. A new long-wave formula for estimating downward clear-sky radiation at the surface. *Q. J. R. Meteorol. Soc.*, **122**(533), 1127–1151.

Savijärvi, H. l991. The United States Great Plains diurnal ABL variation and the nocturnal low-level jet. *Mon. Weather Rev.*, **119**(3), 833–840.

Savijärvi, H. l997. Diurnal winds around Lake Tanganyika. *Q. J. R. Meteorol. Soc.*, **123**(540), 901–918.

Savijärvi, H. and J. Kauhanen. 200l. High resolution numerical simulations of temporal and vertical variability in the stable wintertime boreal boundary layer: a case study. *Theor. Appl. Climatol.*, **70**, 97–103.

Schramm, J. L., M. M. Holland, J. A. Curry and E. E. Ebert. l997. Modeling the thermodynamics of a sea ice thickness distribution. Part 1. Sensitivity to ice thickness resolution. *J. Geophys. Res.*, **102**(C10), 23,079–23,091.

Shine, K. P. l984. Parameterization of shortwave flux over high albedo surfaces as a function of cloud thickness and surface albedo. *Q. J. R. Meteorol. Soc.*, **110**(465), 747–764.

Sturm, M., J. Holmgren, M. König and K. Morris. l997. The thermal conductivity of seasonal snow. *J. Glaciol.*, **43**(143), 26–41.

Vihma, T. l995. Sub-grid parameterization of surface heat and momentum fluxes over polar oceans. *J. Geophys. Res.*, **100**(C11), 22,625–22,646.

Vihma, T. and B. Brümmer. 2002. Observations and modelling of on-ice and off-ice flows in the northern Baltic Sea. *Boundary-Layer Meteorol.*, **103**(1), 1–27.

Vihma, T., J. Hartmann and C. Lüpkes. In press. A case study of an on-ice air flow over the Arctic marginal sea ice zone. *Boundary-Layer Meteorol.*

Wettlaufer, J. S. l991. Heat flux at the ice–ocean interface. *J. Geophys. Res.*, **96**(C4), 7215–7236.